Green Chemistry

PAPER

View Article Online
View Journal | View Issue

Check for updates

Cite this: *Green Chem.*, 2025, **27**, 6796

Asymmetric defective site-triggered triple synergistic modulation in nanoconfined aerogel for superior electrochemical conversion of low-concentration nitrate into ammonia †

Ke Wang, Tong Zhao, Shiyu Zhang, Rupeng Wang, Meng Wang, Zixiang He and Shih-Hsin Ho *

Electrocatalytic conversion of low-concentration nitrate (NO_3^-) into ammonia (NH_3) under ambient conditions is expected to provide an effective solution to the global nitrogen cycle imbalance. However, this process is hindered by slow reaction kinetics and the competing hydrogen evolution reaction (HER). Herein, we anchored oxygen vacancy-containing hollow Co_3O_4 nanoparticles on waste spirulina residue-derived reduced graphene oxide aerogel (Vo-HCo_3O_4@SRGA) for electrocatalytic low-concentration NO_3^- reduction. Finite element simulation demonstrates that the nanoconfined SRGA significantly increases the local concentration of NO_3^-, thereby accelerating the reaction kinetics. Moreover, the Vo is able to disrupt the local structural symmetry of Co–O–Co sites. The asymmetric active site (Vo) can simultaneously enhance NO_3^- adsorption, promote water dissociation, and inhibit hydrogen evolution. Thanks to the triple synergistic modulation of Vo and the nanoconfined effect of SRGA, Vo-HCo_3O_4@SRGA exhibits unprecedented activity (NH_3–N yield rate: 1.53 mg h^{-1} cm^{-2}; NH_3–N Faraday efficiency: 96.5%) superior to most of the reported advanced electrocatalysts under low-concentration NO_3^- conditions. This work cleverly combines macroscopic modification with microscopic fine tuning of catalysts, which is expected to open up new opportunities in the direction of pollutant resourcing.

Received 16th February 2025,
Accepted 12th May 2025

DOI: 10.1039/d5gc00830a

rsc.li/greenchem

Published on 23 2025. Downloaded on 2025/8/7 20:18:34.

Green foundation

1. This work provides an efficient solution for low-concentration nitrate reduction and ammonia synthesis under ambient conditions. By utilizing oxygen vacancy-rich hollow Co_3O_4 nanoparticles anchored on waste spirulina residue-derived graphene oxide aerogel (Vo-HCo_3O_4@SRGA), the combined effects of oxygen vacancies and confinement accelerate reaction kinetics, offering an energy-efficient solution for wastewater treatment and resource recovery. Importantly, the preparation process uses only deionized water instead of toxic organic solvents, making it more environmentally friendly.
2. The catalyst achieves an NH_3–N yield rate of 1.53 mg h^{-1} cm^{-2} and a Faraday efficiency of 96.5%, outperforming many previously reported electrocatalysts.
3. Future research will focus on replacing traditional power sources with solar panels, using renewable energy to create a zero-carbon system for sustainable nitrogen management.

1. Introduction

Nitrate (NO_3^-) has been widely present in industrial wastewater and groundwater in recent years as a result of industrial emissions and agricultural fertilization, and its excessive emission and accumulation can disrupt ecological balance and the global nitrogen cycle.[1–3] The electrocatalytic nitrate reduction reaction (eNO_3^--RR) enables the conversion of aqueous NO_3^- pollutants into value-added ammonia (NH_3) using renewable electricity.[4–7] This approach represents a sustainable win–win strategy for environmental remediation and chemical production. The main research direction of the eNO_3^--RR at present focuses on the exploration of the ideal conditions of high alkaline electrolyte and high NO_3^- concentration.[8–11] Unfortunately, it is almost impossible to find ideal scenarios with both high alkalinity and high NO_3^- concentration in authentic polluted waters, greatly blocking the feasibility of eNO_3^--RR technology in practical applications.[12] Noteworthily, the majority of authentic contaminated water bodies around the globe are typically at low NO_3^- concentration levels

State Key Laboratory of Urban Water Resource and Environment, School of Environment, Harbin Institute of Technology, Harbin, 150040, P. R. China. E-mail: stephen6949@hit.edu.cn

† Electronic supplementary information (ESI) available. See DOI: https://doi.org/10.1039/d5gc00830a

This journal is © The Royal Society of Chemistry 2025

Published on 23 2025. Downloaded on 2025/8/7 20:18:34.

(≤10 mM) with near-neutral pH values.[13] From a practical perspective, directly reducing the low concentration of NO_3^- also helps to avoid high energy consumption that is typically associated with separating and concentrating NO_3^-. However, the slow reaction kinetics is caused by the decrease in the number of reactant molecules and the reduced utilization of active sites at low NO_3^- concentrations. Furthermore, the competing hydrogen evolution reaction (HER) severely limits efficient NO_3^- conversion. Consequently, the development of suitable catalysts to overcome the aforementioned bottlenecks and enhance the NH_3 yield rate and selectivity is a critical issue that requires immediate attention.

Inspired by the nanoconfined effect in natural biological systems (*i.e.*, the cytoskeleton), a remarkable increase in reaction speed and specificity for efficient chemistry is expected to be achieved *via* constructing artificial microscopic nanoconfined spaces.[14–16] Once reactants enter the nanoconfined space, reduced diffusion freedom significantly increases local concentration, thus accelerating the reaction kinetics.[17–19] For example, the nanoconfined effect through graphene aerogel can effectively enrich the reducing intermediates and promote the reduction of Fe(III), resulting in a 208-fold enhancement in the phenol degradation rate constant compared with a system without nanoconfinement.[20] Therefore, we envisage that the unavoidable slow kinetics at low NO_3^- concentrations can be expected to be solved by rationally designing an electrocatalytic system with nanoconfined effect. However, to the best of our knowledge, the application of the graphene aerogel-triggered nanoconfined effect in the eNO_3^--RR has yet to be reported and validated.

In addition, the low catalytic activity due to the competitive HER cannot be ignored. An effective way to inhibit the HER is to regulate the adsorption and binding sites of the hydrogen proton (*H) on the surface of the catalysts. Usually, the asymmetric defect site (Vo) causes uneven spatial distribution of active sites, in turn leading to spatial mismatch between the adsorption and binding sites of *H. This geometric constraint further prevents the proximity and recombination of two *H intermediates into hydrogen.[21] Moreover, this spatial mismatch likewise raises the reactive energy barrier for hydrogen generation, thereby effectively inhibiting the HER.[22,23] In contrast, when *H is adsorbed on active sites with a symmetric structure, the symmetric structure is capable of effectively lowering the reactive energy barrier for the HER through a uniformly distributed electron cloud. Proverbially, the eNO_3^--RR requires a large amount of *H to participate in the reaction, and these *H originate from the dissociation of water molecules. The asymmetry of Vo leads to a distortion of the geometrical configuration of the water molecule *via* altering the local electronic environment and creating an asymmetric electric field. This effect weakens the O–H bond energy and enhances H_2O dissociation probability.[24,25] This asymmetric electric field also exerts a force on NO_3^-, leading to polarity induction and thus enhancing the adsorption process. Here, we uncovered a principal fact that Vo can enhance NO_3^- adsorption, promote water dissociation, and inhibit the HER. Nevertheless, the current literature lacks sufficient information to support Vo-triggered triple synergistic modulation. Furthermore, it has also not been verified whether there is a synergistic co-operation between the nanoconfined effect and Vo.

Herein, we anchored Vo-HCo_3O_4 on the surface of the nanoconfined SRGA to address the kinetic limitations and competing HER issues for the electrocatalytic reduction of low concentrations of NO_3^- to NH_3 under neutral conditions. Notably, the nanoconfined effect generated by the porous skeleton of SRGA significantly enhanced the local NO_3^- concentration, in turn effectively breaking through the slow bottleneck in the kinetic process. Then, the introduced Vo as an asymmetric active site induced a triple synergistic modulation: enhancement of NO_3^- adsorption, promotion of water dissociation and inhibition of the HER. Thanks to the synergistic co-operation of the above efficacies, the Vo-HCo_3O_4@SRGA exhibits remarkable catalytic activity for the conversion of low-concentration NO_3^- into NH_3.

2. Experimental section

2.1. Chemicals

All chemical reagents are described in Text S1.†

2.2. Catalyst preparation

2.2.1. Preparation of Co-MOF@SRGO hydrogels. In a typical synthesis, 20 mg of spirulina-based reduced graphene oxide (SRGO) was first dispersed in 10 mL of deionized water and ultrasonicated for 1 h to ensure uniform dispersion. Then, 184 mg of $Co(CH_3COO)_2{\cdot}4H_2O$, 184 mg of 2-methylimidazole (2-mIM), and 20 mg of carboxymethyl cellulose (CMC) were sequentially added into the SRGO dispersion. Subsequently, the mixture was vigorously processed using a high-speed dispersion machine for 30 min to allow *in situ* growth of the Co-MOF on SRGO to form a homogeneous Co-MOF@SRGO hydrogel. Finally, the Co-MOF@SRGO hydrogel was dialyzed in deionized water for 24 h to remove unreacted precursors and impurities, completing the purification process.

2.2.2. Preparation of Vo-HCo_3O_4@SRGA. The purified Co-MOF@SRGO hydrogels were directly coated on the surface of carbon paper, with the dosage details provided in Table S1.† Following coating, the hydrogel-loaded carbon paper was freeze-dried for 12 h to obtain the Co-MOF@SRGO aerogel (SRGA). Subsequently, the Co-MOF@SRGA composite was pyrolyzed at 800 °C for 2 h under an argon atmosphere to obtain Co@SRGA. Finally, Co@SRGA was thermally treated in a preheated tube furnace (280 °C, O_2/Ar atmosphere) for 30, 90, and 180 min to synthesize Y-Co_3O_4@SRGA, Vo-HCo_3O_4@SRGA and H-Co_3O_4@SRGA, respectively (Y and H represent yolk–shell and hollow structures, respectively). These self-standing electrodes were directly employed for subsequent electrochemical tests.

2.2.3. Preparation of H-Co_3O_4. For comparison, commercial cobalt powder with nanoparticle sizes matching those in H-Co_3O_4@SRGA was employed as a reference. Meanwhile, pure

Published on 23 2025. Downloaded on 2025/8/7 20:18:34.

H-Co_3O_4 was synthesized under identical conditions as H-Co_3O_4@SRGA but without SRGA incorporation, ensuring a controlled evaluation of the role of SRGA in structural evolution.

2.3. Preparation of working electrodes of H-Co_3O_4

First, 21.5 mg of H-Co_3O_4 and 20 μL of 5 wt% Nafion solution were dispersed in a mixture of 655 μL of ethanol and 325 μL of deionized water *via* 60 min ultrasonication to prepare a homogeneous ink. Subsequently, 80 μL of the resulting ink was uniformly coated onto carbon paper (CP, 1 × 1 cm^2) and air-dried at room temperature to complete the electrode fabrication.

2.4. Characterization

More details on the characterization methods are provided in the ESI (Text S2).†

2.5. Electrochemical measurements

The electrochemical measurements were conducted using a CHI 760e electrochemical workstation (Chenhua, Shanghai) in an H-type electrolytic cell. The as-prepared materials, Ag/AgCl electrode, and platinum foil were used as the working electrode, reference electrode, and counter electrode, respectively. The geometric area of the working electrode was set as 1 cm^2. 0.1 M Na_2SO_4 solution (70 mL) was evenly distributed within the cathode and anode chambers, and $NaNO_3$ was added into the cathode compartment containing 140 mg L^{-1} NO_3^--N. All potentials were recorded against a reversible hydrogen electrode (RHE):

$$E_{RHE} = E_{Ag/AgCl} + 0.197\ V + 0.059\ V \times pH$$

Prior to the NO_3^- electroreduction test, the electrolyte was purged with high-purity Ar for 30 min. The scan rates for linear sweep voltammetry (LSV) tests and Tafel slope tests were maintained at 10 mV s^{-1}. Cyclic voltammetry (CV) curves acquired during electrochemical double-layer capacitance (C_{dl}) determinations were measured in a potential window nearly without faradaic processes at different scan rates of 20, 40, 60, 80, and 100 mV s^{-1}. The plot of current density at a given potential against scan rate has a linear relationship, and its slope is C_{dl}. Electrochemical impedance spectra (EIS) were measured in a frequency domain ranging from 10 kHz to 0.1 Hz with a 5 mV perturbation. The chronoamperometry tests were conducted at a series of applied potentials.

2.6. Analytical methods

Detailed information on the determination of nitrogen species concentrations and the calculation of eNO_3^--RR parameters is provided in Text S3 and Text S4,† respectively. Detailed steps of *in situ* Fourier transformed infrared (FT-IR) spectroscopy and online differential electrochemical mass spectrometry (DEMS) measurements are described in Text S5 and Text S6,† respectively. Detailed information on finite element method (FEM) simulations and density functional theory (DFT) calculations are presented in Text S7 and Text S8,† respectively.

3. Results and discussion

3.1. Catalyst characterization

SRGO was prepared according to our previously reported work (Fig. S1†). The preparation procedure for *in situ* growth of Vo-HCo_3O_4@SRGA on carbon paper is shown in Fig. 1a. First, the Co-MOF@SRGO hydrogel was uniformly coated on the surface of carbon paper, and then freeze-dried to obtain Co-MOF@SRGA (Fig. S2†). Subsequently, the obtained Co-MOF@SRGA was subjected to argon pyrolysis (Co@SRGA) and slow oxidation in air to obtain Vo-HCo_3O_4@SRGA. In addition, we optimized the loading amounts of Vo-HCo_3O_4@SRGA on the carbon paper (Fig. S3 and S4†). Scanning electron microscopy (SEM) images clearly demonstrate that Vo-HCo_3O_4 nanoparticles present a highly dispersed distribution in the SRGA backbone without significant agglomeration (Fig. 1b and c and Fig. S5a†). In contrast, pure Vo-HCo_3O_4 undergoes significant sintering under the same conditions (Fig. S5b†), suggesting that the three-dimensional porous network of SRGA limits the migration of Vo-HCo_3O_4 particles, thus enhancing the structural stability of Vo-HCo_3O_4@SRGA. Transmission electron microscopy (TEM) images reveal that Vo-HCo_3O_4 is discretely embedded on the surface of SRGA in the form of hollow nanoparticles with a diameter of approximately 20 nm (Fig. 1d). High-resolution TEM (HRTEM) images show that Vo-HCo_3O_4 exhibited well-defined lattice diffraction fringes with a lattice spacing of 2.43 Å, consistent with the (311) plane of Co_3O_4 (Fig. 1e). Additionally, Vo-HCo_3O_4 contains uniformly distributed elements of Co and O, with the C

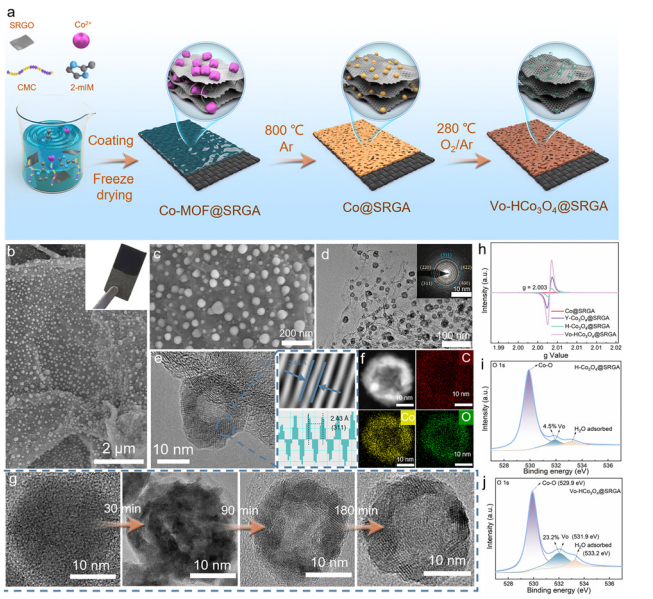

Fig. 1 (a) Schematic illustration of the preparation of Vo-HCo_3O_4@SRGA. (b and c) SEM, (d) TEM, (e) HRTEM, and (f) elemental mapping images of Vo-HCo_3O_4@SRGA. (g and h) TEM and EPR images of Co@SRGA, Y-Co_3O_4@SRGA (30 min), Vo-HCo_3O_4@SRGA (90 min), and H-Co_3O_4@SRGA (180 min). (i and j) High-resolution XPS of O 1s of H-Co_3O_4@SRGA and Vo-HCo_3O_4@SRGA.

This journal is © The Royal Society of Chemistry 2025

Published on 23 2025. Downloaded on 2025/8/7 20:18:34.

element dispersed throughout the entire Vo-HCo_3O_4 structure (Fig. 1f). In order to reveal the evolution of the hollow structure of Vo-HCo_3O_4, Co@SRGA formed by pyrolysis under an argon atmosphere was oxidized in air for different times. As shown in Fig. 1g, Co@SRGA underwent an evolutionary process from solid to yolk–shell to a completely hollow structure. This interesting structural evolution process can be explained *via* the Kirkendall effect.[26] Similarly, solid commercial Co nanoparticles were able to form hollow structures *via* the Kirkendall effect (Fig. S6†).

X-ray diffraction (XRD) and Raman images further confirmed the formation of Co@SRGA consisting of a pure metallic Co phase, Y-Co_3O_4@SRGA consisting of a mixed phase of metallic Co and Co_3O_4, and Vo-HCo_3O_4@SRGA and H-Co_3O_4@SRGA consisting of a pure Co_3O_4 phase (Fig. S7†). In addition to the formation of hollow structures, the Kirkendall effect can produce structural disequilibria in metal oxides through the difference in diffusion rates between the metal and the oxygen, thus contributing to the generation of Vo.[27] Electron paramagnetic resonance (EPR) techniques were applied to probe the presence of Vo in catalysts. Vo-HCo_3O_4@SRGA exhibited the highest EPR signal intensity, suggesting that the concentration of Vo could be effectively controlled by adjusting the oxidation times (Fig. 1h). The high-resolution X-ray photoelectron spectroscopy (XPS) of O 1s demonstrated that Vo-HCo_3O_4@SRGA (90 min) can reach the highest Vo content of 23.2%, which was higher than that for H-Co_3O_4@SRGA (180 min) of 4.5% and Y-Co_3O_4@SRGA (30 min) of 13.1% (Fig. 1i and j and Fig. S8a†). These results demonstrate that the controlled adjustment of oxidation time enables precise construction of different Vo concentrations in the catalysts. Meanwhile, according to the fine-scanned Co 2p XPS spectra, similarly high atomic ratios of Co^{2+}/Co^{3+} can be observed in Y-Co_3O_4@SRGA (1.16) and Vo-HCo_3O_4@SRGA (1.34), which are ascribed to the incompletely oxidized conditions, being consistent with the large number of Vo (Fig. S8b–d†). In sharp contrast, the atomic ratio of Co^{2+}/Co^{3+} in H-Co_3O_4@SRGA decreases to 1.05 because of the oxidation of Co^{2+} to Co^{3+}, leading to the decrease of Vo. The above analyses are consistent with the EPR results, indicating that VoHCo_3O_4@SRGA indeed has the highest concentration of Vo. In addition, the Vo content of H-Co_3O_4 (5.1%) was not significantly different from that of H-Co_3O_4@SRGA, indicating that the introduction of SRGA did not affect the Vo content (Fig. S9†). The photoluminescence (PL) intensity of Vo-HCo_3O_4@SRGA is significantly lower than that of HCo_3O_4@SRGA. This suppression of radiative recombination is attributed to the presence of oxygen vacancies, which serve as electron-trapping centres and effectively inhibit the recombination of electron–hole pairs (Fig. S10†). As shown in Fig. S11,† the work function of Vo-HCo_3O_4@SRGA was significantly lower than that of H-Co_3O_4@SRGA, implying that the introduction of Vo can reduce the work function of the catalysts, thus enhancing the conductivity and reaction activity.[28] The introduction of SRGA greatly extended the specific surface area of H-Co_3O_4@SRGA and Vo-HCo_3O_4@SRGA compared with H-Co_3O_4, providing theoretical support for the enrichment of NO_3^- through the nanoconfined effect (Fig. S12 and Table S2†). In addition, we measured the adsorption capacity of the three catalysts to elucidate the nanoconfined effect of the SRGA framework on NO_3^-. As shown in Fig. S13 and Table S3,† compared with the correlation coefficient values R^2 of the two kinetic models, the pseudo-second-order kinetic model was closer to the experimental data than the pseudo-first-order kinetic model, suggesting that the adsorption process of NO_3^- by the three materials was consistent with the pseudo-second-order kinetic hypothesis. The adsorption capacity and kinetic constants of H-Co_3O_4@SRGA were 2.4 times and 1.9 times those of H-Co_3O_4, respectively. Therefore, SRGA showed an obvious nanoconfined effect on NO_3^-, increased the local concentration of NO_3^- on the catalyst surface, and promoted the reaction kinetics of the electric reduction of NO_3^- to NH_3.

3.2. Electrocatalytic performance for the NO_3^--RR

To evaluate the impact of Vo and the nanoconfined effect of SRGA on the eNO_3^--RR performance, LSV tests were initially conducted in an H-type electrolytic cell. NO_3^-, NO_2^-, and the product NH_3 were detected using an ultraviolet–visible (UV–vis) spectrophotometer (Fig. S14–S16†). The current density of Vo-HCo_3O_4@SRGA with the highest Vo concentration in the NO_3^- electrolyte was greater than that of H-Co_3O_4@SRGA, Co@SRGA, and Y-Co_3O_4@SRGA, indicating that Vo can effectively enhance the eNO_3^--RR process (Fig. 2a). Additionally, the current density of H-Co_3O_4 was found to be significantly

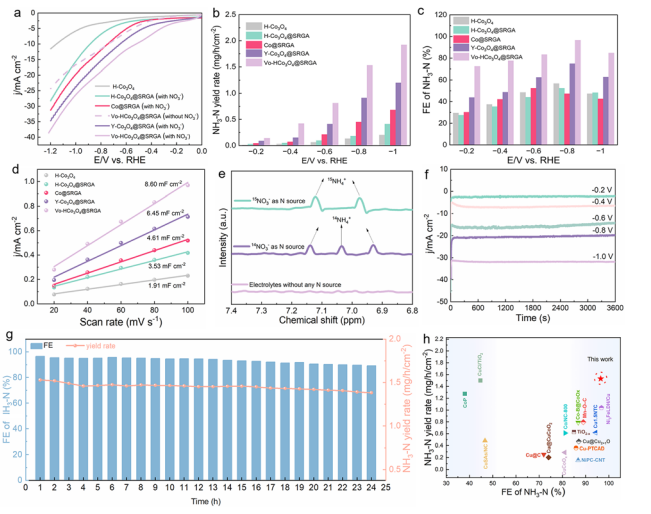

Fig. 2 (a) LSV curves, (b) NH_3-N yield rates, (c) FE, and (d) the fitted linear relationship between the current density and the scan rate of H-Co_3O_4, H-Co_3O_4@SRGA, Co@SRGA, Y-Co_3O_4@SRGA, and Vo-HCo_3O_4@SRGA. (e) ^{1}H-NMR results for NH_4^+ using $^{14}NO_3^-$ and $^{15}NO_3^-$as the N source. (f) The *i*–*t* curves of the Vo-HCo_3O_4@SRGA at various work potentials. (g) Cyclic stability test of Vo-HCo_3O_4@SRGA. (h) Comparison of the eNO_3^--RR performance for Vo-HCo_3O_4@SRGA with some related electrocatalysts under low-concentration NO_3^- conditions.

Published on 23 2025. Downloaded on 2025/8/7 20:18:34.

lower than that of H-Co_3O_4@SRGA, leading to the inference that SRGA with a nanoconfined effect can also contribute to the eNO_3^--RR process. Notably, Vo-HCo_3O_4@SRGA also exhibited the smallest Tafel slope, indicating optimal reaction kinetics (Fig. S17a†). Subsequently, the NH_3-N yield rate of the catalysts was examined at different operating voltages, with Vo-HCo_3O_4@SRGA demonstrating the highest NH_3-N yield rate at all the corresponding voltages (Fig. 2b). The FE of Vo-HCo_3O_4@SRGA exhibited a volcano pattern with decreasing potential (Fig. 2c), indicating a certain starting potential is required for NO_3^- reduction to provide the driving force for the reaction. The subsequent FE decline at more negative potentials originates from the competing HER.[29,30] The FE of Vo-HCo_3O_4@SRGA was the highest at −0.8 V *vs.* RHE (96.5%), corresponding to an NH_3-N yield rate of 1.53 mg h^{-1} cm^{-2}. CV curves at different scan rates were analysed in a non-FE potential window (Fig. S17b–f†). The corresponding C_{dl} values are shown in Fig. 2d, in which the C_{dl} value of Vo-HCo_3O_4@SRGA is larger than that of Y-Co_3O_4@SRGA, H-Co_3O_4@SRGA and Co@SRGA. Since the electrochemically active surface area is proportional to the value of C_{dl}, indicating that Vo increases the electrochemically active surface area, more active sites to facilitate the eNO_3^--RR process are exposed. Furthermore, the C_{dl} value of H-Co_3O_4 was only 1.91 mF cm^{-2} in comparison with H-Co_3O_4@SRGA, indicating that the nanoconfined effect of SRGA also facilitates enhancing the amount of active sites. Vo-HCo_3O_4@SRGA exhibited the smallest Nyquist circle diameter, implying that Vo promotes the electron transfer rate in the eNO_3^--RR process (Fig. S18†). Further comparison of H-Co_3O_4 and H-Co_3O_4@SRGA revealed that SRGA also accelerates the electron transfer rate to some extent. The product NH_3-N was verified to be derived from NO_3^--N by designing blank control experiments with bare carbon paper, an open circuit potential, and no NO_3^- addition. The negligible NH_3-N yield rate under the conditions of the above blank control group experiments verified that the N in NH_3 was derived from NO_3^--N and not from other external contamination (Fig. S19†). The nitrogen changes and reaction processes were traced *via* ^{1}H-nuclear magnetic resonance (^{1}H-NMR). The ^{1}H-NMR peaks of $^{15}NH_4^+$ and $^{14}NH_4^+$ presented double and triple peaks when $^{15}NO_3^-$ and $^{14}NO_3^-$ were used as the N sources, further confirming that the NH_3-N does indeed originate from NO_3^--N rather than from external sources of pollution (Fig. 2e).[31] Before advancing towards practical applications, the stability of the catalysts must be addressed. Fig. 2f illustrates the current *versus* time curves of Vo-HCo_3O_4@SRGA at different operating voltages, and the negligible current density decay indicates the appreciable stability of Vo-HCo_3O_4@SRGA. During 24 consecutive cycles, only the first three cycles revealed a reduced NH_3-N yield rate and FE decay, before remaining largely stable (Fig. 2g). The crystal structure and microscopic morphology showed no obvious change before and after the reaction (Fig. S20†), further illustrating the stability of the structure of Vo-HCo_3O_4@SRGA during the eNO_3^--RR process. To investigate the suitability of Vo-HCo_3O_4@SRGA for different water qualities, the effects of different inorganic anions, inorganic cations and HA on NH_3-N yield rate and FE were also investigated (Fig. S21†). Only a high concentration of Mg^{2+} (10 mM) inhibited the NH_3-N yield rate and FE, with no significant effect of other anions or even high concentrations of HA. In addition, Vo-HCo_3O_4@SRGA exhibited excellent activity in the pH range of 3–11 and NO_3^--N of 50–500 mg L^{-1} (Fig. S22†). All these results indicated the potential applicability of Vo-HCo_3O_4@SRGA under real water conditions. Although the catalytic performance of Vo-HCo_3O_4@SRGA is greatly enhanced by defect and nanoconfined engineering, the difference in performance between Vo-HCo_3O_4@SRGA and other current state-of-the-art catalytic materials is unknown. Therefore, we summarized the performance of some advanced electrocatalytic systems reported in the literature at low concentrations of NO_3^- (Fig. 2h and Table S4†). Among these, Vo-HCo_3O_4@SRGA demonstrated the highest NH_3-N yield rate and FE, highlighting its superior performance as an eNO_3^--RR electrocatalyst.

3.3. FEM and DFT investigation

The nanoconfined effect of SRGA on NO_3^- was successfully verified by finite element method (FEM) simulations (Fig. 3a and b and Fig. S23†). Compared with pure Vo-HCo_3O_4, SRGA@Vo-HCo_3O_4 was able to significantly enhance the localized concentration of NO_3^- due to the nanoconfined effect, thus greatly increasing the accessibility of NO_3^-. This nanoconfined effect contributes to the enhancement of NO_3^- activity in the eNO_3^--RR *via* enriching the localized concentration of NO_3^-, which further facilitates its conversion process to NH_3. Electron localization function (ELF) calculations visualize that Vo formation induces a redistribution of the otherwise uniformly distributed electron density. This

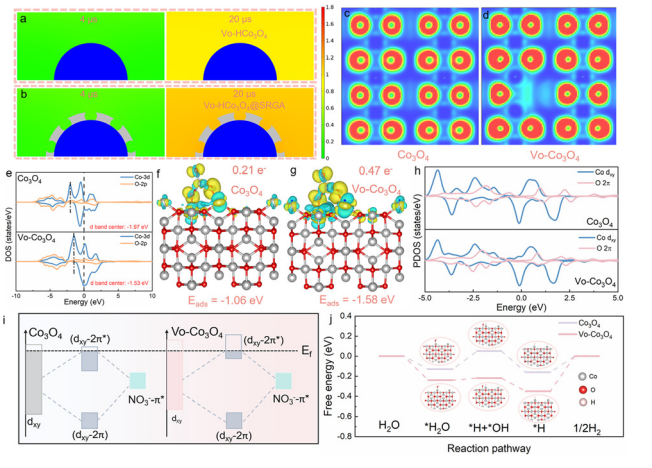

Fig. 3 (a and b) Simulated concentration distribution of NO_3^- on the surface of Vo-HCo_3O_4 and Vo-HCo_3O_4 encapsulated with SRGA at different diffusion times. (c and d) ELF calculations, (e) DOS, (f and g) charge density difference, and (h) PDOS of Co_3O_4 and Vo-Co_3O_4. (i) Spin-down PDOS orbital of d_{xy}−2π* in Co_3O_4/Vo-Co_3O_4-NO_3^-. (j) Free-energy diagrams and corresponding reaction intermediates of water decomposition on Co_3O_4 and Vo-Co_3O_4.

This journal is © The Royal Society of Chemistry 2025

Published on 23 2025. Downloaded on 2025/8/7 20:18:34.

redistribution disrupts the original symmetry, generating a localized asymmetric electronic environment (Fig. 3c and d).[32]

Moreover, the Vo induced inhomogeneity in the Co–O bond length, further reflecting the disruption of the symmetry of the geometry (Fig. S24†). The location of the d-band center is an important theoretical basis for understanding the interaction between the catalyst surface and the reactants.[33,34] Vo raised the d-band center position of Co_3O_4 to −1.53 eV, leading to stronger electron exchange and NO_3^- adsorption (Fig. 3e). Further exploration is needed to elucidate the interaction between NO_3^- and the asymmetric defect sites. To investigate this, the adsorption configurations on the surfaces of Co_3O_4 and Vo-Co_3O_4 were constructed and analyzed (Fig. 3f and g). The adsorption energy (E_{ads}) of NO_3^- on Vo-Co_3O_4 (−1.58 eV) was more negative than that of Co_3O_4 (−1.06 eV), and the charge transfer number between NO_3^- and Vo-Co_3O_4 (0.47 e^-) was higher compared to Co_3O_4 (0.21 e^-). These results demonstrated that Vo can strengthen NO_3^- adsorption and facilitate the electron transfer process.[35] The dense energy band structure of Vo-Co_3O_4 implies a higher density of electronic states compared with Co_3O_4, contributing to a more efficient electron transfer with NO_3^- (Fig. S25†).[36] Accordingly, the interaction between adsorbed NO_3^- and the metal-centered orbitals of Vo-Co_3O_4 was further explored. The d_{xy} orbital of Co and the 2π orbitals of O in NO_3^- manifested a significant overlap in the partial density of states (PDOS) (Fig. 3h and Fig. S26†). This strong interaction triggers the splitting of the bonding and antibonding states. As the d-band center of Vo-Co_3O_4 was close to the Fermi energy level, the d_{xy}–2π* energy levels of bonding and antibonding were subsequently elevated (* represents the antibonding energy level) (Fig. 3i). In this case, the electron occupation of the antibonding state in the NO_3^-/Vo-Co_3O_4 system decreased, enhancing the interaction between NO_3^- and Vo-Co_3O_4.[37,38] Fig. 3j and Fig. S27 and S28† show the Gibbs free energy change (ΔG) plots of Co_3O_4 and Vo-Co_3O_4 in the electrocatalytic HER and the optimized adsorption models of the corresponding intermediates. Vo drastically reduced the dissociation energy barrier of water molecules (0.22 eV to 0.05 eV), promoting easier dissociation of water molecules into H^+ to provide the necessary intermediates for the reaction. In addition, the reaction energy barrier of *H → H_2 for Vo-Co_3O_4 (0.35 eV) was significantly higher than that for Co_3O_4 (0.16 eV), indicating that Vo significantly inhibits the HER side reaction. In summary, the triple synergistic effect (enhanced NO_3^- adsorption, promoted H_2O dissociation, and effectively inhibited HER) of the Vo effectively ensures the high activity and selectivity of Vo-Co_3O_4 in the eNO_3^--RR process.

3.4. Reaction mechanisms and pathway analysis

Two main mechanisms are commonly thought to drive the electrochemical reduction of NO_3^- to NH_3: direct electron transfer and bonding with H^+, and indirect reduction facilitated by H*. The verification of whether H* plays a dominant role in the eNO_3^--RR was done by adding various concentrations of *tert*-butanol (TBA) as a scavenger. Even with the addition of excess TBA, there was no significant change in NO_3^- removal, thus ruling out the H*-mediated pathway (Fig. 4a). Therefore, the main mechanism of Vo-HCo_3O_4@SRGA in the eNO_3^--RR can be identified as direct electron transfer (Fig. 4b). The intermediate products adsorbed on the electrode surface were visualized using *in situ* FT-IR spectroscopy (Fig. 4c). There was no significant difference in the type of absorption peaks of H-Co_3O_4, H-Co_3O_4@SRGA, and Vo-HCo_3O_4@SRGA, suggesting that the presence of SRGA and Vo does not alter the reaction intermediate products (Fig. 4d–f). The broad bands observed at 1650 cm^{-1} and 3300 cm^{-1} are the O–H bending vibrations of water adsorption (δH–O–H) and cleavage (νH–O–H),[39,40] while the bands located at around 1458 cm^{-1} and 1690 cm^{-1} belong to N–H and N–O stretching vibrations, confirming the formation of NH_3 during the eNO_3^--RR process.[41,42] Compared with H-Co_3O_4@SRGA, Vo-HCo_3O_4@SRGA showed a more pronounced signal intensity change with H_2O and related intermediates at more negative potentials. This result suggests that Vo can facilitate H_2O dissociation and NH_3 synthesis. Additionally, online DEMS further clarified that Vo-HCo_3O_4@SRGA generates intermediate products during the eNO_3^--RR (Fig. 4g). The strongest *m*/*z* signal was 17, indicating that Vo-HCo_3O_4@SRGA is able to efficiently electrocatalyze the synthesis of NH_3. Several less intense *m*/*z* signals, such as 14, 15, 16, and 30, which correspond to *N, *NH, *NH_2, and *NO intermediates, confirm the occurrence of the *N hydrogenation pathway. Combined with the above detected intermediates and previous reports, the reaction pathways can be deduced and used for theoretical calculations (Fig. S29†). Fig. 4h shows the ΔG diagrams of Co_3O_4 and Vo-Co_3O_4 in the eNO_3^--RR. For both Co_3O_4 and Vo-Co_3O_4, NH_3 was synthesized by an 8-electron reduction of NO_3^- *via*

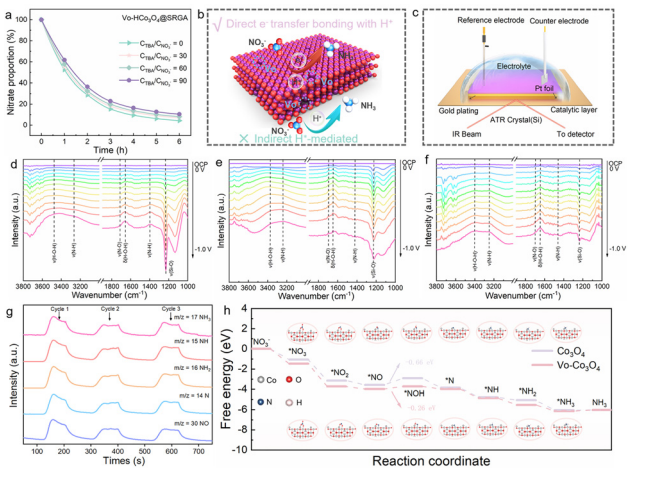

Fig. 4 (a) Time profile of NO_3^- removal curves with or without the addition of TBA. (b) Mechanism schematic diagram of the eNO_3^--RR on Vo-HCo_3O_4@SRGA. (c) Schematic illustration of the *in situ* electrochemical FT-IR. *In situ* FT-IR spectra of (d) H-Co_3O_4, (e) H-Co_3O_4@SRGA, and (f) Vo-HCo_3O_4@SRGA during the eNO_3^--RR. (g) Online DEMS spectra of Vo-HCo_3O_4@SRGA. (h) Free-energy diagrams and corresponding reaction intermediates of the eNO_3^--RR of Co_3O_4 and Vo-Co_3O_4.

Published on 23 2025. Downloaded on 2025/8/7 20:18:34.

the pathway of NO_3^- → *NO_3 → *NO_2 → *NO → *NOH → *N → *NH → *NH_2 → *NH_3 → NH_3 (Fig. S30 and S31†).[43,44] During the whole reaction process, there are two steps with positive ΔG values, which are the *NO hydrogenation (*NO → *NOH) and the desorption of *NH_3 intermediates from the catalyst surface (*NH_3 → NH_3). Because of the high solubility of NH_3 in aqueous solution and the low reaction energy barrier, NH_3 can be readily desorbed from the surface of Co atoms, releasing additional reaction sites.[45,46] Therefore, the rate-determining step (RDS) of the eNO_3^--RR can be considered as *NO → *NOH. Obviously, Vo significantly reduced the reactive energy barrier of the RDS from 0.66 eV to 0.26 eV, improving the efficiency and selectivity of the eNO_3^--RR.

4. Conclusions

In summary, we successfully anchored Vo-HCo_3O_4 obtained *via* the Kirkendall effect to the surface of SRGA. The porous skeleton of SRGA can improve the accessibility of the active sites. It also significantly increases the local NO_3^- concentration due to a unique nanoconfined effect, thereby accelerating the reaction kinetics. *In situ* FT-IR spectroscopy and DFT calculations demonstrate that Vo induced a triple synergistic modulation: enhancement of NO_3^- adsorption, promotion of water dissociation, and inhibition of the HER. Furthermore, the introduction of Vo raised the bonding and antibonding energy levels of d_{xy}–2π* in NO_3^-/Vo-Co_3O_4 and lowered the reaction energy barrier of RDS (*NO → *NOH), facilitating the adsorption and activation of NO_3^-. As a result, Vo-HCo_3O_4@SRGA exhibited a considerable NH_3-N yield rate (1.53 mg h^{-1} cm^{-2}), Faraday efficiency (96.5%), and selectivity (97.2%) in the conversion of low-concentration NO_3^- to NH_3. This work highlights the design principles of advanced electrocatalysts for low-concentration NO_3^- conversion, providing solutions for resource recovery of NO_3^--containing wastewater. We believe that this creative work has the opportunity to be extended to other electrocatalytic reactions in the aqueous phase, in addition to being generous in the eNO_3^--RR.

Author contributions

Ke Wang and Tong Zhao: data curation and writing – original draft. Shiyu Zhang: investigation. Rupeng Wang: formal analysis. Meng Wang: writing – review & editing. Zixiang He: supervision. Shih-Hsin Ho: funding acquisition.

Data availability

The authors confirm that the data supporting the findings of this study are available within the article and its ESI.†

Conflicts of interest

There are no conflicts to declare.

Acknowledgements

This work was financially supported by the National Natural Science Foundation of China (No. 52070057).

References

1 D. R. Kanter, O. Chodos, O. Nordland, M. Rutigliano and W. Winiwarter, *Nat. Sustainability*, 2020, **3**, 956–963.
2 B. Zhang, Z. Dai, Y. Chen, M. Cheng, H. Zhang, P. Feng, B. Ke, Y. Zhang and G. Zhang, *Nat. Commun.*, 2024, **15**, 2816.
3 J. Sun, S. Garg, J. Xie, C. Zhang and T. D. Waite, *Environ. Sci. Technol.*, 2022, **56**, 17298–17309.
4 F.-Y. Chen, Z.-Y. Wu, S. Gupta, D. J. Rivera, S. V. Lambeets, S. Pecaut, J. Y. T. Kim, P. Zhu, Y. Z. Finfrock, D. M. Meira, G. King, G. Gao, W. Xu, D. A. Cullen, H. Zhou, Y. Han, D. E. Perea, C. L. Muhich and H. Wang, *Nat. Nanotechnol.*, 2022, **17**, 759–767.
5 S. Han, H. Li, T. Li, F. Chen, R. Yang, Y. Yu and B. Zhang, *Nat. Catal.*, 2023, **6**, 402–414.
6 X. Chen, Y. Cheng, B. Zhang, J. Zhou and S. He, *Nat. Commun.*, 2024, **15**, 6278.
7 B. Zhou, Y. Tong, Y. Yao, W. Zhang, G. Zhan, Q. Zheng, W. Hou, X.-K. Gu and L. Zhang, *Proc. Natl. Acad. Sci. U. S. A.*, 2024, **121**, e2405236121.
8 W. Liao, J. Wang, G. Ni, K. Liu, C. Liu, S. Chen, Q. Wang, Y. Chen, T. Luo, X. Wang, Y. Wang, W. Li, T.-S. Chan, C. Ma, H. Li, Y. Liang, W. Liu, J. Fu, B. Xi and M. Liu, *Nat. Commun.*, 2024, **15**, 1264.
9 J. Suh, H. Choi, Y. Kong and J. Oh, *Adv. Sci.*, 2024, **11**, 2407250.
10 J.-J. Zhang, Y.-Y. Lou, Z. Wu, X. J. Huang and S.-G. Sun, *J. Am. Chem. Soc.*, 2024, **146**, 24966–24977.
11 N. C. Kani, N. H. L. Nguyen, K. Markel, R. R. Bhawnani, B. Shindel, K. Sharma, S. Kim, V. P. Dravid, V. Berry, J. A. Gauthier and M. R. Singh, *Adv. Energy Mater.*, 2023, **13**, 2204236.
12 K.-H. Kim, H. Lee, X. Huang, J. H. Choi, C. Chen, J. K. Kang and D. O'Hare, *Energy Environ. Sci.*, 2023, **16**, 663–672.
13 P. H. van Langevelde, I. Katsounaros and M. T. M. Koper, *Joule*, 2021, **5**, 290–294.
14 Y. Chen, M. Zuo, Y. Chen, P. Yu, X. Chen, X. Zhang, W. Yuan, Y. Wu, W. Zhu and Y. Zhao, *Nat. Commun.*, 2023, **14**, 5229.
15 Y. Huang, J. Ren and X. Qu, *Chem. Rev.*, 2019, **119**, 4357–4412.
16 J. Zhang, Z. Wang, X. Lin, X. Gao, Q. Wang, R. Huang, Y. Ruan, H. Xu, L. Tian, C. Ling, R. Shi, S. Xu, K. Chen and Y. Wu, *Angew. Chem., Int. Ed.*, 2025, **64**, e202416686.

 This journal is © The Royal Society of Chemistry 2025

Published on 23 2025. Downloaded on 2025/8/7 20:18:34.

17 W. Qu, M. Luo, Z. Tang, T. Zhong, H. Zhao, L. Hu, D. Xia, S. Tian, D. Shu and C. He, *Environ. Sci. Technol.*, 2023, **57**, 13205–13216.
18 S. Zhang, M. Sun, T. Hedtke, A. Deshmukh, X. Zhou, S. Weon, M. Elimelech and J.-H. Kim, *Environ. Sci. Technol.*, 2020, **54**, 10868–10875.
19 Q. V. Ly, L. Cui, M. B. Asif, W. Khan, L. D. Nghiem, Y. Hwang and Z. Zhang, *Water Res.*, 2023, **230**, 119577.
20 X. Zhang, J. Tang, L. Wang, C. Wang, L. Chen, X. Chen, J. Qian and B. Pan, *Nat. Commun.*, 2024, **15**, 917.
21 L. Wu, Z. Wang, J. Liu, C. Liu, X. Li, Y. Zhang, W. Wang, J. Ma and Z. Sun, *Appl. Catal., B*, 2024, **343**, 123526.
22 Q. Cheng, M. Huang, L. Xiao, S. Mou, X. Zhao, Y. Xie, G. Jiang, X. Jiang and F. Dong, *ACS Catal.*, 2023, **13**, 4021–4029.
23 W. Zhong, Z. Gong, Z. He, N. Zhang, X. Kang, X. Mao and Y. Chen, *J. Energy Chem.*, 2023, **78**, 211–221.
24 X. Chen, J. Chen, H. Chen, Q. Zhang, J. Li, J. Cui, Y. Sun, D. Wang, J. Ye and L. Liu, *Nat. Commun.*, 2023, **14**, 751.
25 Z. Wei, M. Zhao, Z. Yang, X. Duan, G. Jiang, G. Li, F. Zhang and Z. Hao, *Proc. Natl. Acad. Sci. U. S. A.*, 2023, **120**, e2217148120.
26 J. Zhu, W. Tu, H. Pan, H. Zhang, B. Liu, Y. Cheng, Z. Deng and H. Zhang, *ACS Nano*, 2020, **14**, 5780–5787.
27 D. Ji, L. Fan, L. Tao, Y. Sun, M. Li, G. Yang, T. Q. Tran, S. Ramakrishna and S. Guo, *Angew. Chem., Int. Ed.*, 2019, **58**, 13840–13844.
28 Y. Zhang, Y. Lin, T. Duan and L. Song, *Mater. Today*, 2021, **48**, 115–134.
29 K. Chu, W. Zong, G. Xue, H. Guo, J. Qin, H. Zhu, N. Zhang, Z. Tian, H. Dong, Y.-E. Miao, M. B. J. Roeffaers, J. Hofkens, F. Lai and T. Liu, *J. Am. Chem. Soc.*, 2023, **145**, 21387–21396.
30 Y. Xiong, Y. Wang, C. C. Tsang, J. Zhou, F. Hao, F. Liu, J. Wang, S. Xi, J. Zhao and Z. Fan, *Environ. Sci. Technol.*, 2024, **58**, 10863–10873.
31 Y. Wang, H. Li, W. Zhou, X. Zhang, B. Zhang and Y. Yu, *Angew. Chem., Int. Ed.*, 2022, **61**, e202202604.
32 W. Lyu, Y. Liu, J. Zhou, D. Chen, X. Zhao, R. Fang, F. Wang and Y. Li, *Angew. Chem., Int. Ed.*, 2023, **62**, e202310733.
33 S. Zhang, R. Wang, K. Wang, M. Wang, Z. He, H. Chen and S.-H. Ho, *Environ. Sci. Technol.*, 2024, **58**, 1921–1933.
34 L. Li, X. Zhang, M. Humayun, X. Xu, Z. Shang, Z. Li, M. F. Yuen, C. Hong, Z. Chen, J. Zeng, M. Bououdina, K. Temst, X. Wang and C. Wang, *ACS Nano*, 2024, **18**, 1214–1225.
35 K. Wang, R. Mao, R. Liu, J. Zhang, H. Zhao, W. Ran and X. Zhao, *Nat. Water*, 2023, **1**, 1068–1078.
36 H. Du, H. Guo, K. Wang, X. Du, B. A. Beshiwork, S. Sun, Y. Luo, Q. Liu, T. Li and X. Sun, *Angew. Chem.*, 2023, **135**, e202215782.
37 S. Yang, X. Guo, X. Li, T. Wu, L. Zou, Z. He, Q. Xu, J. Zheng, L. Chen, Q. Wang and Z. J. Xu, *Angew. Chem., Int. Ed.*, 2024, **63**, e202317957.
38 G. Qian, W. Lyu, X. Zhao, J. Zhou, R. Fang, F. Wang and Y. Li, *Angew. Chem., Int. Ed.*, 2022, **61**, e202210576.
39 M. Xie, G. Zhu, H. Yang, B. Liu, M. Li, C. Qi, L. Wang, W. Jiang, P. Qiu and W. Luo, *Adv. Energy Mater.*, 2024, **14**, 2401717.
40 J. Li, H. Li, K. Fan, J. Y. Lee, W. Xie and M. Shao, *Chem. Catal.*, 2023, **3**, 100638.
41 Y. Huang, C. He, C. Cheng, S. Han, M. He, Y. Wang, N. Meng, B. Zhang, Q. Lu and Y. Yu, *Nat. Commun.*, 2023, **14**, 7368.
42 J. Ni, J. Yan, F. Li, H. Qi, Q. Xu, C. Su, L. Sun, H. Sun, J. Ding and B. Liu, *Adv. Energy Mater.*, 2024, **14**, 2400065.
43 A. Zhu, H. Liu, S. Bu, K. Liu, C. Luan, D. Lin, G. Gan, Y. Zhou, T. Zhang, K. Liu, G. Hong, H. Li and W. Zhang, *ACS Nano*, 2024, **18**, 22344–22355.
44 S. Lu, G. Lin, H. Yan, Y. Li, T. Qi, Y. Li, S. Liang and L. Jiang, *ACS Catal.*, 2024, **14**, 14887–14894.
45 H. Y. Zhou, Y. B. Qu, J. C. Li, Z. L. Wang, C. C. Yang and Q. Jiang, *Appl. Catal., B*, 2022, **305**, 121023.
46 Z. Meng, J.-X. Yao, C.-N. Sun, X. Kang, R. Gao, H.-R. Li, B. Bi, Y.-F. Zhu, J.-M. Yan and Q. Jiang, *Adv. Energy Mater.*, 2022, **12**, 2202105.